Russian Journal of Earth Sciences

Automatic Identification of Ocean Eddies in SAR Using U-Net Convolutional Neural Network

V. I. Tuchinskaya[1], I. L. Bashmachnikov[*,1,2,4], N. Yu. Zakhvatkina[2,3], I. E. Kozlov[4], and D. A. Iakovleva[2]

[1]Saint Petersburg State University, Saint Petersburg, Russia
[2]Nansen International Environmental and Remote Sensing Center, Saint Petersburg, Russia
[3]Arctic and Antarctic Research Institute, Saint Petersburg, Russia
[4]Marine Hydrophysical Institute of RAS, Sevastopol, Russia
* **Correspondence to:** Igor Bashmachnikov, igorb1969@mail.ru

Abstract: The effect of mesoscale and submesoscale eddies on regional heat and freshwater transport, sea-ice dynamics, and bioproductivity in polar and subpolar regions is largely unknown. The promising massive investigation of relatively small polar and subpolar eddies with Synthetic Aperture Radar (SAR) images requires robust automatic algorithms for their identification. Following recent advances in such algorithms for Sentinel-1 data, in this study describes an algorithm for identifying mesoscale and submesoscale eddies in earlier Envisat Wide-Swath SAR images using convolutional neural network based on U-Net architecture. The model was trained on 520 fragments of SAR images 512 × 512 pixels each, collected in the Greenland, Irminger and Labrador Seas. The resulting accuracy of eddy detection was 0.89. An improvement in the segmentation accuracy compared to previous studies was a result of the applied annotation methods, based on the analysis of typical texture patterns and morphological characteristics of ocean eddies in SAR. The developed algorithm showed its potential in identification of eddies not only in the Marginal Ice Zone, but also in the open water.

Keywords: automatic eddy detection, Envisat SAR images, U-Net convolutional neural network

Citation: Tuchinskaya V. I., Bashmachnikov I. L., Zakhvatkina N. Yu., Kozlov I. E., and Iakovleva D. A. (2026), Automatic Identification of Ocean Eddies in SAR Using U-Net Convolutional Neural Network, *Russian Journal of Earth Sciences*, 26, ES1006, EDN: ZFIMQY, https://doi.org/10.2205/2026es001084

1. Introduction

Being abundant in the ocean, eddies play a critical role in the ocean energy balance, enstrophy exchange between ocean scales, influencing the large-scale ocean circulation [*Bower et al.*, 2002; *Hirschi et al.*, 2020; *Luo and Lu*, 2000; *Meneghello et al.*, 2017]. Eddy transport of heat and salt significantly affects regional ocean heat and freshwater balance, as well as the ocean-atmosphere exchange [*Barbero et al.*, 2010; *Bashmachnikov et al.*, 2023; *Golivets and Koshlyakov*, 2003; *Wunsch and Ferrari*, 2004].

The study of mesoscale eddy dynamics is one of the challenging tasks in particular at high latitudes, where eddy scales are often too small to be resolved in the widely used satellite altimetry data [*Bashmachnikov et al.*, 2020; *Chelton et al.*, 2011; *Morozov and Kozlov*, 2023; *Raj and Halo*, 2016]. The use of high resolution Synthetic Aperture Radar (SAR), Sea-Surface Temperature (SST) and Ocean Color (OC) images provide high-quality data with the potential to conduct massive analysis of eddy parameters at smaller scales than the altimetry data allow, significantly expanding our understanding of eddy dynamics and their impact on exchange of mass, heat, and salt in the ocean [*Aguedjou et al.*, 2023; *Bashmachnikov et al.*, 2015; *Bashmachnikov et al.*, 2020; *Gaube et al.*, 2013; *Lavrova et al.*, 2011; *Siegelman et al.*, 2020]. The spatial coverage of high-resolution SST and OC images (1 × 1 km or better) is limited by the cloud cover, especially frequent at high latitude

Research Article

Received: May 27, 2025
Accepted: November 10, 2025
Published: March 10, 2026

regions. SAR data has high potential as they combine high-resolution data (dozens of metes) with the ability of the signal to penetrate through the cloud cover.

SAR data are available from a range of satellites (ERS, Envisat, Sentinel-1 and other) most often operate at the C-band (wavelengths of 4–8 cm) and typically has various polarizations. The SAR data represent the backscattering intensity of the radio signal (also referred to as image brightness) that varies depending on changes of the type and physical state of the reflecting surface (water, ice or land) and with its orientation to the SAR radar beam. In the areas with low ice concentrations of the Marginal Ice Zone (MIZ), sea-ice is used as a tracer for ocean eddy detection, due to usually strong differences of the radio wave reflectance from the sea-ice and open water [*Cassianides et al.*, 2021; *Khachatrian et al.*, 2023; *Kozlov et al.*, 2020; *Wu et al.*, 2025]. For the open water the intensity of the reflected C-band signal depends mainly on the intensity of capillary waves (ripples), the wavelength of which is of the same order as that of the radio wave [*Johannessen et al.*, 2005]. In such areas, the eddy structures can be observed with the slick or shear-wave mechanisms [*Karimova*, 2012]. For the slick mechanism, image contrasts are formed as a result of convergence/divergence of the mean currents and due to suppression of gravity-capillary waves by sea-surface films typically of natural origin. The latter are concentrated in the convergence zones of ocean currents, decreasing reflectance intensity of the signal compared to the surrounding area. Shear-wave mechanism is a result of interaction of the gravity-capillary waves with the shear ocean currents. Influenced by a combination of various factors, which include currents of different origin (eddy-related, Ekman, tidal, long-wave, etc.) and effects of bottom topography, the eddies, visualized due to the shear-wave, typically are more difficult to detect in SAR images compared to eddies detected due to the slick mechanism. For all mechanisms, the visibility of eddies also depends on the SAR viewing angle, wind strength, wind direction and other factors [*Johannessen et al.*, 2005; *Kudryavtsev et al.*, 2005]. Thus, manifestation of eddies in SAR images is expected at the wind velocity range from 2–3 $\mathrm{m \cdot s^{-1}}$ to 12 $\mathrm{m \cdot s^{-1}}$, while the highest contrasts in SAR images are observed with the wind speeds of 3–5 $\mathrm{m \cdot s^{-1}}$ [*Karimova*, 2012; *Wang et al.*, 2019]. Too weak winds do not form ripples, while at strong winds the intensive wind wave mixing and formation of foam strips mask the mesoscale current patterns linked to eddy dynamics.

Despite the limitations above, SAR signal penetrates the cloud cover which forms its main benefit for massive detection of mesoscale and submesoscale eddies compared to data in other frequency bands. However, predominantly visual way of identification of eddies in SAR images [*Atadzhanova et al.*, 2017; *Ginzburg et al.*, 2017; *Karimova*, 2012; *Kozlov et al.*, 2019] does not allow obtaining massive eddy statistics, except for limited water areas and time periods. Algorithms for automatic identifying and tracking of ocean eddies in SAR images still remains an issue in oceanographic research.

Deep learning is a powerful tool that can automate and optimize the processes of object identification and data classification. In several recent studies the convolutional neural network (CNN) techniques were successfully used for detection of ocean eddies. For example, [*Xia et al.*, 2022] and [*Zi et al.*, 2024] detect oceanic eddies in Sentinel-1 radar images using Context and Edge Association Network (CEA-Net) and You Only Look Once (YOLO) CNNs. [*Khachatrian et al.*, 2023; *Wu et al.*, 2025] used a pre-trained YOLO model to identify eddies in Sentinel-1 images in the marginal ice zone, where the presence of broken sea-ice significantly simplifies the task of identifying ocean eddies. There is probably the only study by [*Xu et al.*, 2023] that describes an automatic method of eddy detection in SAR images from ERS-2 and Envisat, using used the two-unit stacking architecture – Stacked Attention Network (SANet). However, such attempts are isolated and each new successful application of CNN to the problem of identifying ocean eddies in SAR images represents an innovative approach that has a potential for application in monitoring and analysis of ocean processes. This study represents an implementation of a CNN algorithm for the automatic identification of ocean eddies in Envisat images with U-Net convolutional neural network (CNN) architecture. Over 10 years of Envisat data (2002–2012) allow the potential

extension of the emerging SAR-derived eddy datasets in Sentinel-1 data (from 2014 on) over previous decades.

2. Materials and Methods

Identification of mesoscale and submesoscale eddies was carried out using Advanced SAR (ASAR) images from Envisat satellite available at the ESA Data Portal Earth Observation Data Service Portal (https://esar-ds.eo.esa.int/). The Wide Swath Mode images acquired in C-band and HH polarization provides a swath of around 400 km with a spatial resolution of 150 m. The study area covers the western areas of the Greenland, Irminger and Labrador Seas, including (but not limited to) the MIZ (Figure 1).

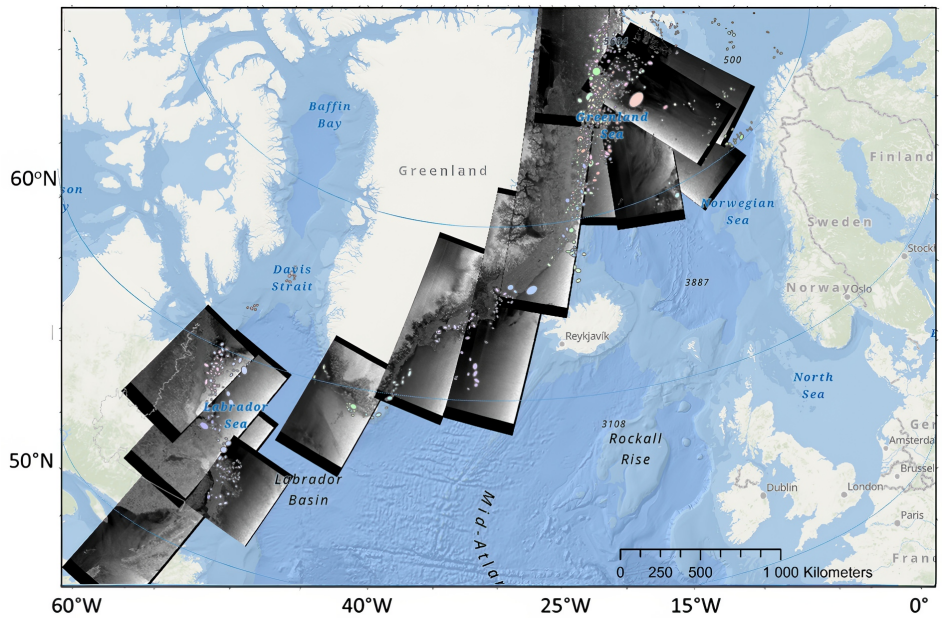

Figure 1. The study region with radar images used in this study. Eddies used in the training, testing and validation samples are marked with colored light circles.

The eddy centers, as well as the major and minor semi-axes of the eddy approximation with an ellipse, were visually identified [see *Kozlov et al.*, 2019, for details]. It should be noted that the visual method of detecting eddy structures may be subjective since eddy spiral patterns may not be well pronounced and eddy boundaries often are blurred.

U-Net architecture is widely used for image segmentation, due to its ability to effectively identify complex structures, such as ocean eddies in SAR images. Pre-processing of Envisat ASAR images included standard procedure of elimination of the areas associated with land and packed sea-ice, radiometric calibration to backscatter values and their conversion to decibels (dB). Further an angular correction is done, which corrects the brightness decrease with the distance from the satellite track, thus, bringing the entire SAR image to the limited range of brightness values [*Kalinin and Tolmacheva*, 2005; *Sea Ice...*, 2020]. Next, filtering was applied to reduce the spatial resolution of the image for a reduction of the speckle noise. To eliminate the areas with high ice concentration from the analysis, Advanced Microwave Scanning Radiometer (AMSR) Sea Ice product (https://data.seaice.uni-bremen.de/amsre/) at 3×3 km spatial resolution was used as a reference dataset of large-scale distribution of sea ice, where ice and water is separated [*Spreen et al.*, 2008]. The AMSR data were interpolated to the SAR spatial resolution using the methods of the nearest neighbor. The areas with concentration less than an empirical threshold of 85% sea-ice concentration were filtered out to minimize the presence of large contiguous areas of drifting ice near the ice edge. The next step of the pre-processing includes normalization of pixel values, which is limiting the original range of backscatter values in SAR images to a predefined range (-28 dB, 0 dB), in order to assure a more

stable and rapid convergence of the training process. Finally, the original images were divided into tiles of predefined size of 512 × 512 pixels. For the training dataset eddies with well-defined elliptical boundaries and contrasting texture were annotated. This approach allows avoiding inclusion of noise and ambiguous peripheral areas into the area of an eddy and increases the accuracy of eddy identification when their contours are not clearly distinguishable from the background. The size and shape of all eddies were defined; their unique morphological and textural features were annotated.

Eddies on SAR images often have complex asymmetric shapes, including spiral and circular structures, and a complex texture. In the central areas of such eddies, visualized due to ice mechanism, dense and homogeneous core areas are often observed. They are identified on radar images due to the brightness of their elliptical cores (or their inner/outer parts) that differ significantly from the background (Figure 2b,c). Sometimes, however, such eddies may not have strong contrasts with the background, but can be detected due to their numerous spiral or circular structures, which create a significant contrast with the internal areas, as well as with the background (Figure 2a). Such eddies are identified and annotated based on these linear features of high texture contrast along their boundaries. Eddies, which manifest themselves on SAR images due to slick mechanism, seldom have relatively homogeneous and contrasting central cores and are distinguished due to well-defined spiral patterns (Figure 2d–f). Boundaries of such eddies are less clearly defined then in the previous case. Eddies, manifesting themselves in SAR due to shear wave mechanism are the most difficult to identify (Figure 2g–i). They do not have a contrasting core and their spiral structures show weak-contrast obscured with intensive noise. Still distinguished by their spiral patterns, such eddies do not have clear contrasting boundary their sizes could be derived only approximately.

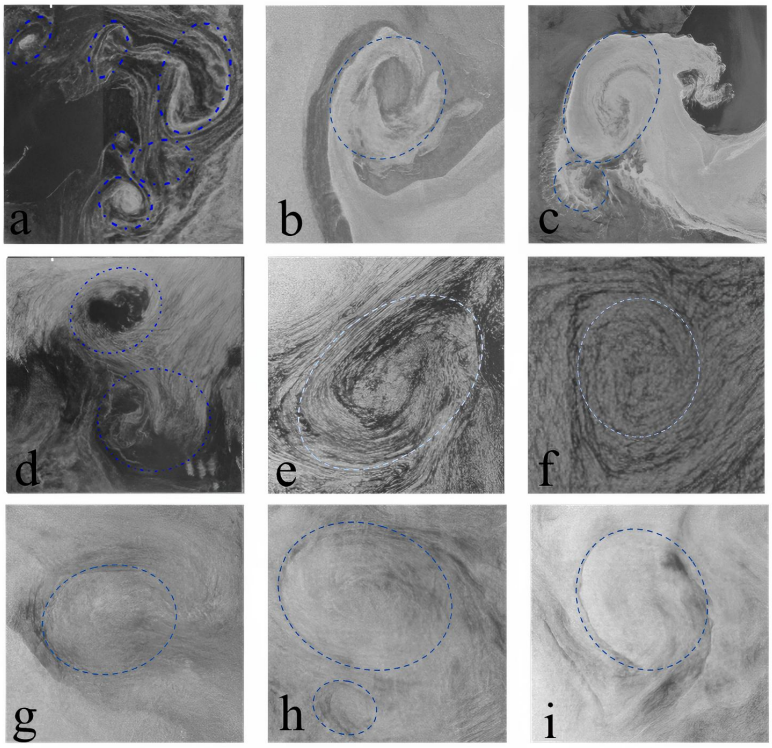

Figure 2. Manifestation of eddy structures on Envisat SAR images by means of: (a–c) ice mechanism: a) Envisat ASAR 02/18/2007 01:16 GMT; b) Envisat ASAR 04/18/2007 14:08 GMT, c) Envisat ASAR 05/12/2007 11:22 GMT) (d–f) slick mechanism: Envisat ASAR 06/08/2007 10:33 GMT, (g–i) shear-wave mechanism: g) Envisat ASAR 07.08.2007 12:31 GMT; h–i) Envisat ASAR 06/19/2007 19:46 GMT.

After the pre-processing, the SAR images were divided into non-overlapping fixed-size tiles of 512×512 pixels which form the training dataset. Training on relatively small image fragments allowed for enhancing the training dataset ensuring stable training of the model on small, but representative image fragments (tiles), as well as efficient use of the computer video memory resources. A total of 520 tiles of 512×512 pixels were analysed. In each of the tile at least one eddy was visually detected. 400 tiles were used for training and testing and the remaining 120 tiles were used for validation. These tiles were additionally used to enhance the training dataset using data augmentation methodology. After augmentation the training dataset increased by around 4 times. The augmentation includes typical transformations: rotations of fragments by a randomly selected angle, horizontal and vertical flipping and changes in the image contrast (contrast values vary either from 0.5 to 2.1 or from 0.4 to 1.5 depending on the brightness range of the original image). The augmentation also allows for a better balancing of the original dataset and increasing its diversity, which helps to improve the generalization ability of the CNN algorithm and makes it more robust to different oceanic conditions, variations in the image geometry and quality.

CNN based semantic segmentation divides the original image into semantically meaningful regions by assigning a corresponding class label to each pixel. In our case, during segmentation all image pixels were divided into 3 classes: land and compact ice, background areas of water and sparse ice, and eddies. The training of a CNN allows finding the optimal weights of the operator which maps the image from the pixel brightness space to the object class space while minimizing the loss function. To achieve this, the U-Net architecture was selected, which includes determining the configuration of the parameters of the convolutional layers; selecting the activation functions, optimization algorithm and regularizer; adjusting the training hyperparameters, such as the learning rate, weight initialization, the number of training epochs, and the number of training subsets. The CNN architecture for image segmentation tasks includes the following components (Figure 3): a contracting path (encoder) and a symmetric expanding path (decoder), which are linked by a series of intermediate connections [*Ronneberger et al.*, 2015]. The encoder is a stack of convolutional layers that gradually reduces the dimensionality of the input image and extracts features that are important for the desired segmentation. This allows to reduce the dimensionality of the feature space by removing redundant information and compacting the extracted features. The decoder, on the contrary, consists of transposed convolutional layers. It gradually increases the dimensionality of features and constructs the segmented image. The use of the 'skip connections' mechanism between the encoder and decoder allows to directly transfer information about the spatial details of the original image during image reconstruction, which helps to avoid a loss of details. This is useful for segmenting images with uneven contours of the derived objects.

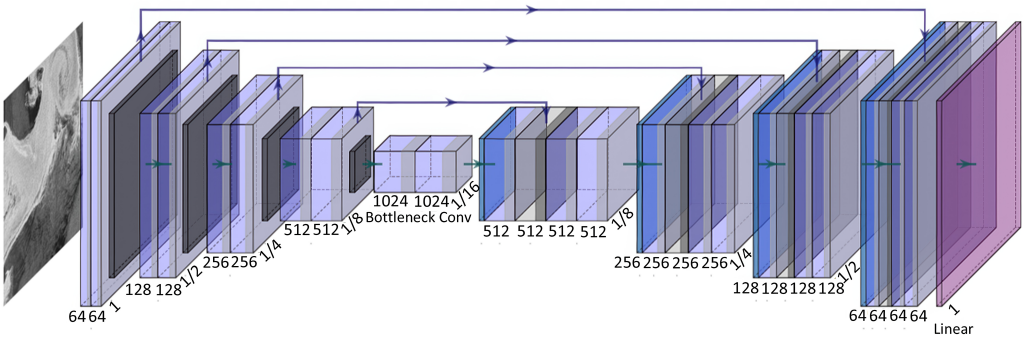

Figure 3. U-Net architecture. On the left is the original image and the encoder, on the right is the decoder and the segmented image. The blue arrows conventionally indicate the operation of the 'skip connections' mechanism.

The loss function is defined as: $L(y, \hat{p}) = -\sum y_i \cdot \log(\hat{p}_i)$, where y_i is the true value of the integer class label i, $\hat{p}_i$ is the predicted probability of this value of the class label i. The loss function estimates the discrepancy between the true and predicted values of class labels, characterizing the accuracy of image segmentation. The model is trained or fitted with a gradient descent algorithm minimizing the loss function to reduce the error between the predicted and true class labels. The Adam (Adaptive Moment Estimation) optimization algorithm was used to avoid overtraining. It updates the model parameters by minimizing the expected value of the stochastic objective function from the model weights. Backpropagation was used to update the weights and biases in the CNN to minimize the error, calculated as a function of differences between the CNN output and the real values. The learning rate determines the size of the steps with which the network weights are updated within the gradient descent process. The choice and adjustment of the learning rate directly affect the convergence of the model. In this study, a learning rate was chosen to be in the range of $1–4 \times 10^{-5}$ unit, which ensures a slow but stable convergence. This choice is justified by the desire to carefully approximate the optimal model parameters. The number of training epochs was chosen to be equal to 100. This ensures a sufficient number of iterations for the model to converge to the optimal weights. Ridge regularization was used, for which a quadratic penalty on the model coefficients was added to the original cost function, which helps to prevent overfitting by limiting the absolute values of the parameters.

The performance of the CNN model was assessed based on the analysis of metric indicators and the analysis of intermediate predictions. After a visual analysis of the image segmentation results, the quality of the segmentation eddies was assessed using the Accuracy (Ac) and Intersection over Union (IoU) metrics.

Ac was defined as the proportion of correctly classified pixels among the total number of pixels:

$$\mathrm{Ac} = \frac{TP + TN}{TP + TN + FP + FN},$$

where TP (True Positive) – correctly predicted target class labels; TN (True Negative) – correctly predicted background class labels; FP (False Positive) – incorrectly predicted target class labels; FN (False Negative) – incorrectly predicted background class labels. This metric provides a generalized assessment of the ability of the model to correctly classify pixels and demonstrates the overall model performance.

IoU metric provides a more accurate assessment of the segmentation quality for each class, especially in the case of unbalanced sampling. IoU measures the degree of overlap between the predicted and true eddy segments:

$$\mathrm{IoU} = \frac{\text{Area of Overlap}}{\text{Area of Union}}.$$

It estimates the ratio of the intersection area of true and predicted segments to the area of their union, which allows for a more accurate assessment of the segmentation quality, especially in the case of complex objects with a heterogeneous structure.

To reduce errors in determining the contours of the selected eddies, series of post-processing procedures for the segmentation results were carried out. The Suzuki–Abe algorithm was used to isolate the contours of the eddies [*Suzuki and Abe*, 1985], which allows tracking and extracting the boundaries of objects in binarized images. The algorithm is based on pixel-by-pixel analysis of the image to isolate the vertices of the object, preserving only the main points of the horizontal, vertical and diagonal segments of the contours of an object derived using CNN. Further, the obtained set of measures is used for an approximation of the object (eddy) by an ellipse. The coordinates of the eddy center and the sizes of its semi-axes were stored.

3. Results

Figure 4 illustrates the results of segmentation of ice-driven ocean eddies, showing different morphologies and levels of complexity of the original images. Visualization of the set of pixels identified as eddies compared to those identified with visual analysis (Figure 4, last column).

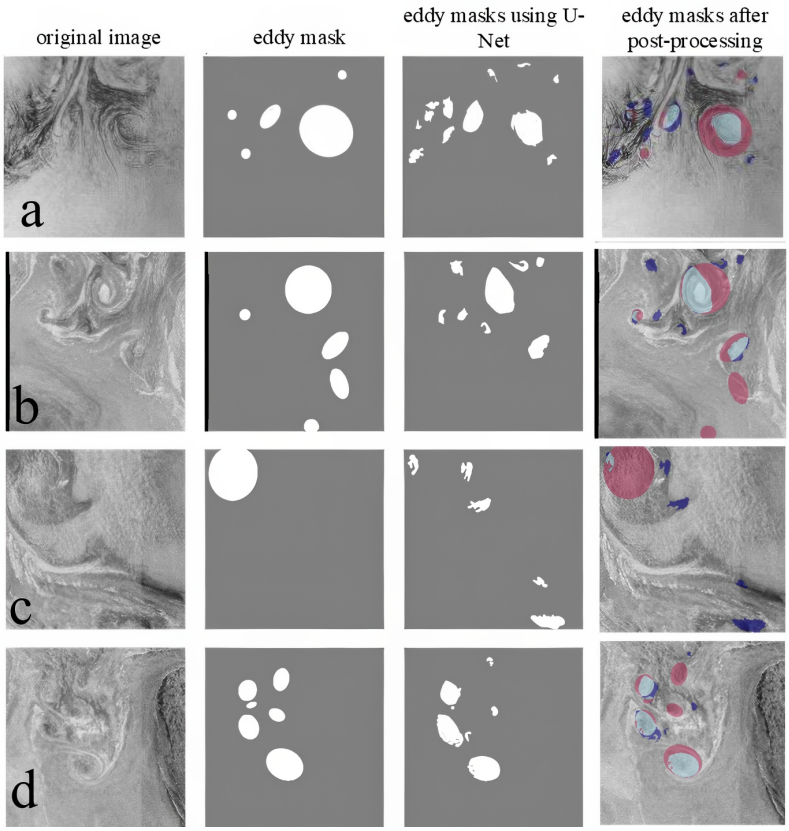

Figure 4. Examples of segmentation of a group of images with an ice mechanism of manifestation on Envisat SAR images (a–d). 1st column – original images, 2nd column – visually identified eddies (white), 3rd column – areas classified as eddies by the U-Net model (white), 4th column – results of post-processing (approximation of eddy contours by ellipses); eddy areas identified visually are shown in red, using U-Net is shown in blue, both visually and using U-Net are shown in light blue.

The eddies with smooth, clear, continuous contours and uniform texture were clearly identified by the algorithm (Figure 4a). Large and small eddies with complex morphology (Figure 4b,d) have an ambiguous and variable texture with round or elongated elliptical shapes. Inside the large eddy (Figure 4b) with a clearly defined center, stripes and spiral elements are visible, indicating high texture complexity. Smaller eddies (Figure 4b,d) have a non-uniform texture with various details and less clear boundaries. The most difficult to identify was a large eddy with blurred boundaries and a complex internal texture with a high noise component (Figure 4c). Besides the annotated eddies, several "False Positive" eddies were identified (dark blue in Figure 4). Detailed examination suggests that these features, although were not identified visually, have structural element that suggest these may be blurred small eddies. The model, however, miss some of the eddies identified visually or does not always detect eddy boundaries correctly (red areas in Figure 4b–d).

The numerical evaluation of the model performance showed that the U-Net achieves high pixel classification accuracy with an Ac = 0.89, indicating a good ability of the model to correctly differentiate eddy patterns from the background. However, the moderately high value of IoU = 0.57 indicates the presence of errors in defining eddy size (eddy boundaries). Still this is above that obtained by [*Xu et al.*, 2023] for Envisat data. A decrease in IoU metrics is a result of high variability of eddy textures and shapes, as well as of a limited size of the training dataset.

A detailed analysis of performance of the algorithm demonstrates that U-Net algorithm correctly identifies eddies with homogeneous textures and simple structure of spiral contours, which leads to its high accuracy. The quality of eddy recognition by the model decreases for blurred spiral structures with low contrast between the eddy core and the background and for high original images with a high noise level. The latter includes the presence of strong small-scale texture inhomogeneities containing many small features, stripes, spiral elements and variations in brightness between the neighboring pixels. This is often characteristic for areas with a number of small neighboring eddies.

As a testing data, Envisat ASAR image from August 9 2007 in the Fram Strait region was used to assess the statistical characteristics of ocean eddies along the East Greenland Current (Figure 5). In the image, 49 well pronounced ocean eddies were visually identified and 34 eddies were identified by the U-Net algorithm. 27 eddies were identified by both methods. Note that, although most of the eddies were correctly identified in the MIZ (in the north-western part of the image), a number of eddies were also detected in the open water. This is expected as the MIZ eddies often clear spiral signals in SAR images (Figure 2).

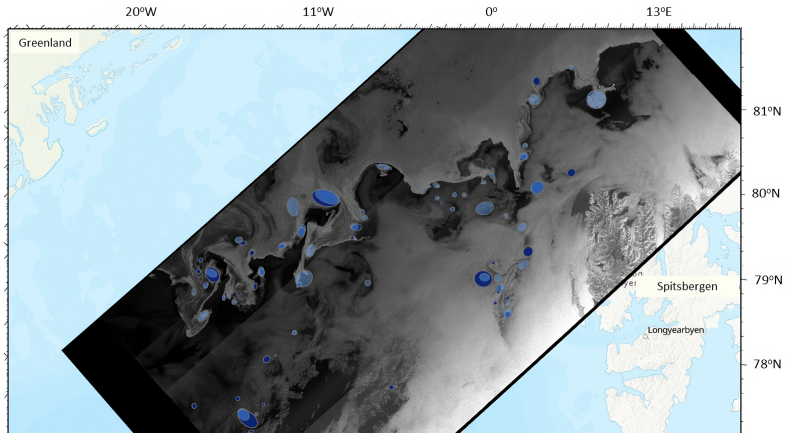

Figure 5. Eddies structures in an Envisat ASAR image from 09.08.2007: manually identified eddies are marked in blue and eddies, identified by the automatic U-Net algorithm are marked in light blue.

The radii of 27 eddies, visually and automatically identified in Figure 5, varied from 2–4 km to 25 km (Figure 6). The average radius of these eddies in U-Net results was almost the same as for the visually detected eddies (12 km against 11 km). This somewhat exceeds the first baroclinic radius of the Rossby deformation, which varies across the study region between 4–8 km [*Nurser and Bacon*, 2014]. The correlation of the radii of 27 eddies (identified both visually and automatically) was 0.9 for this image. However, due to the abovementioned difficulties in determining the eddy boundaries, the difference in the radii between the original and detected individual eddies ranges from 0.1 km to 14 km.

4. Conclusions

In this study, an algorithm for identifying ocean eddies in SAR images was developed using a CNN based on the U-Net architecture. Over 520 tiles from Envisat ASAR images, collected in the Greenland, Irminger and Labrador Seas, were used for model training and validation. The developed algorithm showed high accuracy in eddy detection of 0.89. Experiments with various annotation methods based on the analysis of texture patterns and morphological characteristics led to an improvement in the segmentation accuracy compared to the previous studies, where Envisat data were used. The developed algorithm is able to identify eddies not only in MIZ, but also in the open water, where detecting eddies are less clearly pronounced in SAR images. This demonstrates significant progress in SAR image processing capabilities. The recognition process revealed a tendency of the U-Net algorithm to detect some small eddies with the radii of several kilometers, which were not visually detected. Although some of these small eddies are true eddies, some represent artifacts. This is a result of a complex structure of the background currents,

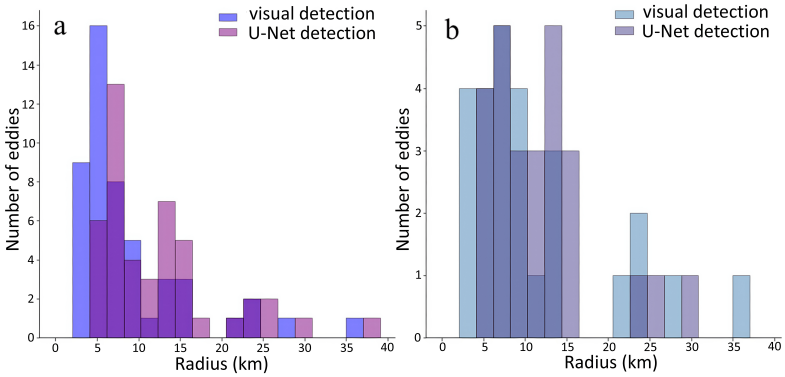

Figure 6. Histograms of eddy radii from the Envisat ASAR image from 09.08.2007: a) all eddies detected visually and with U-Net algorithm; b) a subset of intersecting eddies, detected visually and with U-Net algorithm.

which negatively affect the overall detection accuracy. It was also noted that closely located eddies were sometimes combined in the U-Net output into larger structures, indicating a superfluous sensitivity of the model to small details. This indicates the need to improve this part of the algorithm, in particular for the open water part of the study region. Further improvement of the identification accuracy requires revising the data annotation methods to exclude elements that introduce noise, as well as an increase in the quantity of rare structures to more accurately balance the training dataset.

Acknowledgments. Development of AI-based automated eddy detection algorithm was supported by Russian Science Foundation grant 25-17-00309, https://rscf.ru/project/25-17-00309/. Analysis and manual identification of eddies in historical SAR data was done within state task FNNN-2024-0017

References

Aguedjou H. M. A., Chaigneau A., Dadou I., et al. Imprint of mesoscale eddies on air-sea interaction in the tropical Atlantic Ocean // Remote Sensing. — 2023. — Vol. 15, no. 12. — P. 3087. — https://doi.org/10.3390/rs15123087.

Atadzhanova O. A., Zimin A. V., Romanenkov D. A., et al. Satellite radar observations of small eddies in the White, Barents and Kara Seas // Physical Oceanography. — 2017. — No. 2. — P. 75–83. — https://doi.org/10.22449/1573-160x-2017-2-75-83.

Barbero L., González-Dávila M., Santana-Casiano J. M., et al. Variability of the water mass transports and fluxes in the eastern North Atlantic during 2001 // Journal of Geophysical Research: Oceans. — 2010. — Vol. 115, no. C3. — https://doi.org/10.1029/2008jc005212.

Bashmachnikov I., Neves F., Calheiros T., et al. Properties and pathways of Mediterranean water eddies in the Atlantic // Progress in Oceanography. — 2015. — Vol. 137. — P. 149–172. — https://doi.org/10.1016/j.pocean.2015.06.001.

Bashmachnikov I. L., Kozlov I. E., Petrenko L. A., et al. Eddies in the North Greenland Sea and Fram Strait from satellite altimetry, SAR and high-resolution model data // Journal of Geophysical Research: Oceans. — 2020. — Vol. 125, no. 7. — e2019JC015832. — https://doi.org/10.1029/2019jc015832.

Bashmachnikov I. L., Raj R. P., Golubkin P., et al. Heat transport by mesoscale eddies in the Norwegian and Greenland seas // Journal of Geophysical Research: Oceans. — 2023. — Vol. 128, no. 2. — e2022JC018987. — https://doi.org/10.1029/2022jc018987.

Bower A. S., Le Cann B., Rossby T., et al. Directly measured mid-depth circulation in the northeastern North Atlantic Ocean // Nature. — 2002. — Vol. 419, no. 6907. — P. 603–607. — https://doi.org/10.1038/nature01078.

Cassianides A., Lique C. and Korosov A. Ocean eddy signature on SAR-derived sea ice drift and vorticity // Geophysical Research Letters. — 2021. — Vol. 48, no. 6. — e2020GL092066. — https://doi.org/10.1029/2020gl092066.

Chelton D. B., Schlax M. G. and Samelson R. M. Global observations of nonlinear mesoscale eddies // Progress in Oceanography. — 2011. — Vol. 91, no. 2. — P. 167–216. — https://doi.org/10.1016/j.pocean.2011.01.002.

Gaube P., Chelton D. B., Strutton P. G., et al. Satellite observations of chlorophyll, phytoplankton biomass, and Ekman pumping in nonlinear mesoscale eddies // Journal of Geophysical Research: Oceans. — 2013. — Vol. 118, no. 12. — P. 6349–6370. — https://doi.org/10.1002/2013jc009027.

Ginzburg A. I., Krek E. V., Kostianoy A. G., et al. Evolution of mesoscale anticyclonic vortex and vortex dipoles/multipoles on its base in the south-eastern Baltic (satellite information: May-July 2015) // Journal of Oceanological Research. — 2017. — Vol. 45, no. 1. — P. 10–22. — https://doi.org/10.29006/1564-2291.jor-2017.45(1).3. — (In Russian).

Golivets S. V. and Koshlyakov M. N. Cyclonic eddies at the Subantarctic front and formation of the Antarctic intermediate water // Oceanology. — 2003. — Vol. 43, no. 3. — P. 305–317. — EDN: LHULBT.

Hirschi J. J.-M., Barnier B., Böning C., et al. The Atlantic meridional overturning circulation in high-resolution models // Journal of Geophysical Research: Oceans. — 2020. — Vol. 125, no. 4. — e2019JC015522. — https://doi.org/10.1029/2019jc015522.

Johannessen J. A., Kudryavtsev V., Akimov D., et al. On radar imaging of current features: 2. Mesoscale eddy and current front detection // Journal of Geophysical Research: Oceans. — 2005. — Vol. 110, no. C7. — https://doi.org/10.1029/2004jc002802.

Kalinin N. A. and Tolmacheva N. I. Space research methods in meteorology. — Perm : Perm State University, 2005. — 348 p. — EDN: QKFKIZ ; (in Russian).

Karimova S. S. Spiral eddies in the Baltic, Black and Caspian seas as seen by satellite radar data // Advances in Space Research. — 2012. — Vol. 50, no. 8. — P. 1107–1124. — https://doi.org/10.1016/j.asr.2011.10.027.

Khachatrian E., Sandalyuk N. and Lozou P. Eddy detection in the marginal ice zone with Sentinel-1 data using YOLOv5 // Remote Sensing. — 2023. — Vol. 15, no. 9. — P. 2244. — https://doi.org/10.3390/rs15092244.

Kozlov I. E., Artamonova A. V., Manucharyan G. E., et al. Eddies in the Western Arctic Ocean from spaceborne SAR observations over open ocean and marginal ice zones // Journal of Geophysical Research: Oceans. — 2019. — Vol. 124, no. 9. — P. 6601–6616. — https://doi.org/10.1029/2019jc015113.

Kozlov I. E., Plotnikov E. V. and Manucharyan G. E. Brief Communication: Mesoscale and submesoscale dynamics of marginal ice zone from sequential SAR observations // The Cryosphere Discussions. — 2020. — P. 1–11. — https://doi.org/10.5194/tc-2020-126.

Kudryavtsev V., Akimov D., Johannessen J., et al. On radar imaging of current features: 1. Model and comparison with observations // Journal of Geophysical Research: Oceans. — 2005. — Vol. 110, no. C7. — https://doi.org/10.1029/2004jc002505.

Lavrova O. Yu., Kostianoy A. G., Lebedev S. A., et al. Complex satellite monitoring of the Russian seas. — Moscow : Space Research Institute of RAS, 2011. — 470 p. — (In Russian).

Luo D. and Lu Y. The influence of negative viscosity on wind-driven, barotropic ocean circulation in a subtropical basin // Journal of Physical Oceanography. — 2000. — Vol. 30, no. 5. — P. 916–932. — https://doi.org/10.1175/1520-0485(2000)030<0916:tionvo>2.0.co;2.

Meneghello G., Marshall J., Cole S. T., et al. Observational inferences of lateral eddy diffusivity in the halocline of the Beaufort Gyre // Geophysical Research Letters. — 2017. — Vol. 44, no. 24. — P. 12331–12338. — https://doi.org/10.1002/2017gl075126.

Morozov E. A. and Kozlov I. E. Eddies in the Arctic Ocean revealed from MODIS optical imagery // Remote Sensing. — 2023. — Vol. 15, no. 6. — P. 1608. — https://doi.org/10.3390/rs15061608.

Nurser A. J. and Bacon S. The Rossby radius in the Arctic Ocean // Ocean Science. — 2014. — Vol. 10, no. 6. — P. 967–975. — https://doi.org/10.5194/os-10-967-2014.

Raj R. P. and Halo I. Monitoring the mesoscale eddies of the Lofoten Basin: importance, progress, and challenges // International Journal of Remote Sensing. — 2016. — Vol. 37, no. 16. — P. 3712–3728. — https://doi.org/10.1080/01431161.2016.1201234.

Ronneberger O., Fischer P. and Brox T. U-Net: Convolutional Networks for Biomedical Image Segmentation // Medical Image Computing and Computer-Assisted Intervention - MICCAI 2015. — Springer International Publishing, 2015. — P. 234–241. — https://doi.org/10.1007/978-3-319-24574-4_28.

Sea Ice in the Arctic: Past, Present and Future / ed. by O. M. Johannessen, L. P. Bobylev, E. V. Shalina, et al. — Springer International Publishing, 2020. — https://doi.org/10.1007/978-3-030-21301-5.

Siegelman L., Klein P., Riviére P., et al. Enhanced upward heat transport at deep submesoscale ocean fronts // Nature Geoscience. — 2020. — Vol. 13, no. 1. — P. 50–55. — https://doi.org/10.1038/s41561-019-0489-1.

Spreen G., Kaleschke L. and Heygster G. Sea ice remote sensing using AMSR-E 89-GHz channels // Journal of Geophysical Research: Oceans. — 2008. — Vol. 113, no. C2. — https://doi.org/10.1029/2005jc003384.

Suzuki S. and Abe K. Topological structural analysis of digitized binary images by border following // Computer Vision, Graphics, and Image Processing. — 1985. — Vol. 30, no. 1. — P. 32–46. — https://doi.org/10.1016/0734-189x(85)90016-7.

Wang Y., Yang M. and Chong J. Simulation and Analysis of SAR Images of Oceanic Shear-Wave-Generated Eddies // Sensors. — 2019. — Vol. 19, no. 7. — P. 1529. — https://doi.org/10.3390/s19071529.

Wu J., Zheng Y., Wang T., et al. Oriented ice eddy detection network based on the Sentinel-1 dual-polarization data // Frontiers in Marine Science. — 2025. — Vol. 11. — https://doi.org/10.3389/fmars.2024.1480796.

Wunsch C. and Ferrari R. Vertical mixing, energy, and the general circulation of the oceans // Annual Review of Fluid Mechanics. — 2004. — Vol. 36, no. 1. — P. 281–314. — https://doi.org/10.1146/annurev.fluid.36.050802.122121.

Xia L., Chen G., Chen X., et al. Submesoscale oceanic eddy detection in SAR images using context and edge association network // Frontiers in Marine Science. — 2022. — Vol. 9. — https://doi.org/10.3389/fmars.2022.1023624.

Xu M., Li H., Yun Y., et al. End-to-end pixel-wisely detection of oceanic eddy on SAR images with stacked attention network // IEEE Journal of Selected Topics in Applied Earth Observations and Remote Sensing. — 2023. — Vol. 16. — P. 9711–9724. — https://doi.org/10.1109/jstars.2023.3322404.

Zi N., Li X. M., Gade M., et al. Ocean eddy detection based on YOLO deep learning algorithm by synthetic aperture radar data // Remote Sensing of Environment. — 2024. — Vol. 307. — P. 114139. — https://doi.org/10.1016/j.rse.2024.114139.